Achieving Long-Range Arbitrary Uniform Alignment of Nanostructures in Magnetic Fields

Viney Ghai,* Santosh Pandit, Magnus Svensso, Ragnar Larsson, Aleksandar Matic, Roselle Ngaloy, Saroj P. Dash, Ann Terry, Kim Nygård, Ivan Mijakovic, and Roland Kádár*

For magnetic field orientation of nonstructures to become a viable method to create high performance multifunctional nanocomposites, it is of paramount importance to develop a method that is easy to implement and that can induce long-range uniform nanostructural alignment. To overcome this challenge, inspired by low field nuclear magnetic resonance (NMR) technology, a highly uniform, high field strength, and compact magnetic-field nanostructure orientation methodology is presented for polymeric nanocomposites using a Halbach array, for the first time. Potential new advances are showcased for applications of graphene polymer composites by considering their electro-thermal and antibacterial properties in highly oriented orthogonal morphologies. The high level of anisotropy induced in the graphene nanocomposites studied stands out through: 1) up to four decades higher electrical conductivities recorded in comparison to their randomly oriented counterparts, at concentrations where the latter show minimal improvements compared to the unfilled polymer; 2) over 1200% improvement in thermal conductivity, 3) antibacterial surfaces at field benchmark levels with lower filler content and with the added versatility of arbitrary orientation of the nanofillers. Overall, the new method and variations thereof can open up new horizons for tailoring nanostructure and performance for virtually all major nanocomposite applications based on graphene and other types of fillers.

1. Introduction

The nanofiller revolution of the past few decades has created enormous potential to enhance and / or impart novel multifunctional properties in polymeric composite materials.[1–4] Graphene (2D), and its entire family of variants, nanoclays (2D), nanotubes (1D), nanocellulose systems (1D), hexagonal boron nitride (2D), and the recent explosion MXenes,[5] continue to provide the possibility of fine-tuning specific properties in composites. However, because the vast majority of high aspect ratio fillers are anisotropic whenever a nanostructure interacts with an imposed field, flow fields being the most common during manufacturing operations, orientation will be induced, resulting in anisotropic nanocomposite properties that will directly impact their performance. Aligning nanomaterials in arbitrary specific orientations is the key to a wide range of valuable applications, such as energy storage,[6,7] water purification,[8] antibacterial,[9] optical absorbers,[10,11] sensors[12] gas barriers, and

V. Ghai, R. Larsson, R. Kádár
Industrial and Materials Science
Chalmers University of Technology
Göteborg 41296, Sweden
E-mail: ghai@chalmers.se; roland.kadar@chalmers.se
S. Pandit, I. Mijakovic
Department of LIfe Sciences
Chalmers University of Technology
Göteborg 41296, Sweden
M. Svensso
Wellspect HealthCare
Aminogatan 1, Mölndal 43121, Sweden

A. Matic
Department of Physics
Chalmers University of Technology
Göteborg 41296, Sweden
R. Ngaloy, S. P. Dash
Department of Microtechnology and Nanoscience
Chalmers University of Technology
Göteborg 41296, Sweden
A. Terry, K. Nygård, R. Kádár
MAX IV Laboratory
Lund University
Lund 22484, Sweden
I. Mijakovic
The Novo Nordisk Foundation Center for Biosustainability
Technical University of Denmark
Kongens Lyngby 2800, Denmark

**ADVANCED
SCIENCE NEWS**

www.advancedsciencenews.com

**ADVANCED
FUNCTIONAL
MATERIALS**

www.afm-journal.de

thermal interface materials.[13] Without orientation, such applications are not possible, and yet, ensuring adequate orientation especially for medium and large-scale processes has remained a challenge.[14–16]

In general, there are four main approaches to achieving nanomaterial orientation: by 1) flow fields, shear, and extensional,[16–19] 2) electric field,[20] 3) magnetic field,[21] and 4) spatial confinement in thin films.[22] Flow-based techniques, while ubiquitous in polymer processing, are predominantly limited to unidirectional orientation in the flow direction, which may be detrimental to the desired properties. Spatial confinement is similarly limited in alignment direction and is also constraining in terms of sample dimensions. Meanwhile, alignment with electric fields requires rather large voltages, making it difficult to implement in laboratory and manufacturing settings. Advances in the magnetic field orientation of graphene can be found in a recent review by Ghai et al., 2024.[16] Among these, the use of magnetic fields to align nanomaterials could stand out with exceptional potential compared to the other two methods provided that a reasonably high magnetic field could be generated in a compact form and be capable of sweeping alignment of nanomaterials with upscaling potential.

Briefly, to date, two magnetic field systems have been employed for nanomaterial orientation: using permanent magnets and electromagnets.[21,23] Although capable of generating higher magnetic fields, the utilization of electromagnets comes with challenges because of the intricate control of high-voltage electric currents and other associated drawbacks. As a result, the use of permanent magnets, in single or dual configurations, has become the preferred focus for orienting nanomaterials in the field.[24,25] In particular, while a static magnetic field with a single or dual magnet configuration can effectively align 1D nanomaterials, the same approach falls short for 2D nanomaterials due to their increased degree of freedom.[16,26] This requires an alternative strategy for aligning 2D nanomaterials such as graphene, MXenes, and boron nitride, etc. Thus, a rotational magnetic field generated by a dual magnet configuration has emerged as the most successful approach in this context.[26,27] Regardless, a significant challenge persists in the inherent non-uniformity of the magnetic field even in dual magnet systems due to the curvature of magnetic field lines.[16] This non-uniformity hampers the desired long-range uniform alignment of nanomaterials, presenting a bottleneck in realizing the full potential of oriented nanomaterial systems. Addressing this challenge requires the innovation of a new magnet configuration design.

A most prominent 2D material, graphene, a single layer of carbon atoms arranged in a hexagonal lattice,[28,29] is known as a wonder material due to its remarkable electrical and thermal conductivity, etc. Therefore, graphene has led to extensive research and holds promise across domains spanning electronics, biomedical, and energy storage, among others.[30,31] However, graphene exhibits distinct properties along varying crystallographic directions, with differing electrical and thermal conductivities and mechanical strengths. Therefore, the orientation of graphene is essential in many applications because it can significantly influence the material's properties and performance. Importantly, the precise alignment of graphene sheets enables the strategic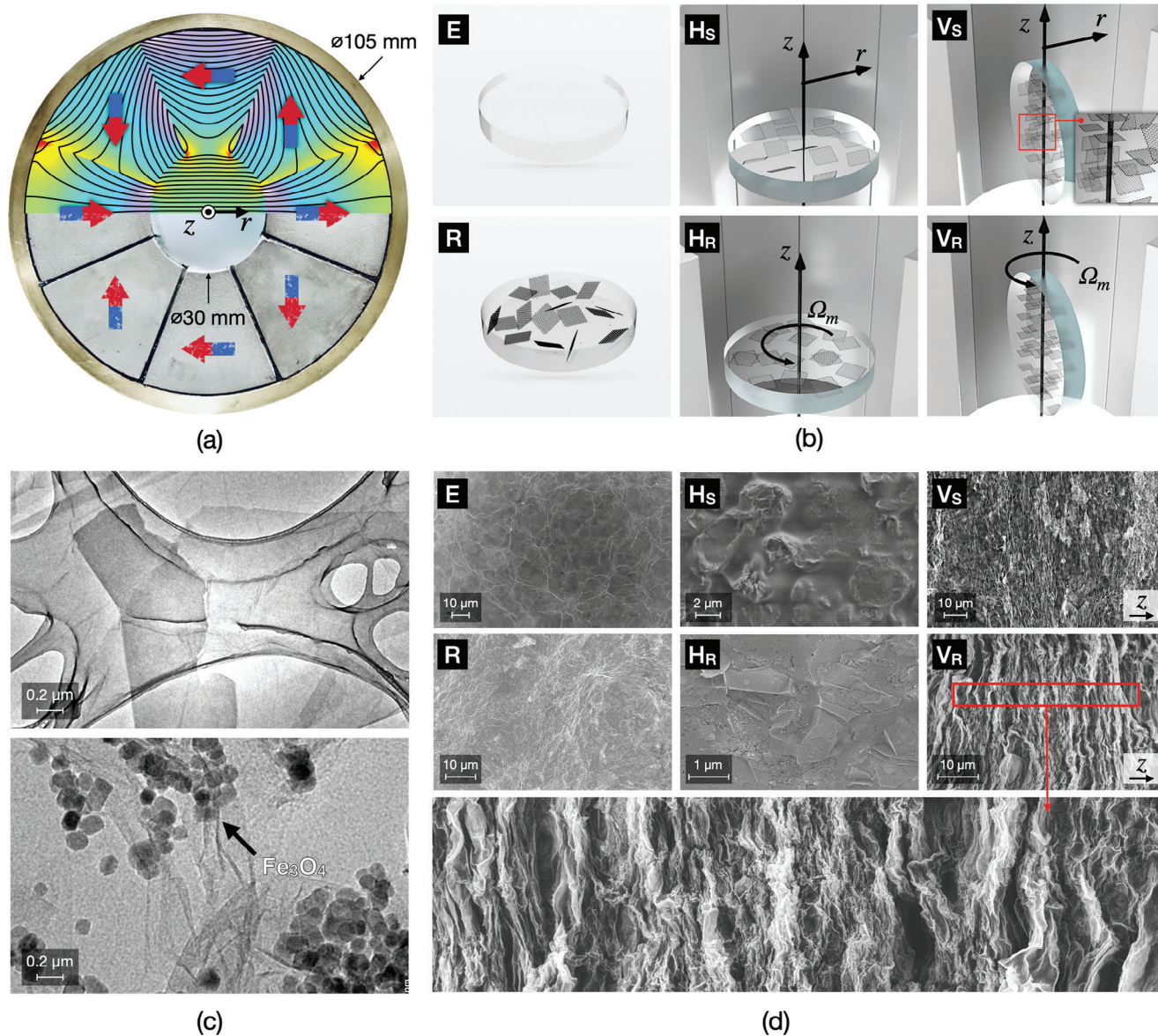 utilization of these directional properties for tailored applications. Inspired by advances in low-field NMR technology[32] and their potential for inline use,[33,34] this work seeks to attain a compact, versatile, ultra-high magnetic field orientation cell with exceptional magnetic field uniformity using a Halbach array,[35,36] **Figure 1a** and Figure S3 (Supporting information). We tailor polymer nanocomposites in orthogonal orientational configurations using magnetostatic and magnetodynamic conditions (rotating magnetic field), Figure 1b, based on epoxy (E), a widely-used engineering thermoset, reduced graphene oxide (rGO) doped with iron oxide nanoparticles Fe_3O_4 ($rGO_{(m)}$), Figure 1c. As a testament to the orientation efficacy of the Halbach array orientation cell, see Figure 1d, we explore the unique performance of the nanocomposites in terms of anisotropy, electrical, thermal and antibacterial properties. The present study thus not only fills a critical gap in the field of nanomaterial alignment but also has the potential to revolutionize a wide array of applications and industries.

2. Results and Discussion

To design an innovative configuration for aligning nanomaterials using magnetic fields, a comprehensive study of various Halbach array designs has been conducted using numerical modeling, see Section S1 (Supporting information). Among the different array configurations explored, the trapezoidal arrangement exhibited the highest magnetic field strength while maintaining a constant inner radius (15 mm) or volume, see Figure S1 (Supporting information).

It has been previously established that pristine graphene is inherently diamagnetic and thus requires ultra-high magnetic fields of more than 10 T to align.[16] However, generating such intense magnetic fields for large-scale production of graphene-aligned composites poses considerable challenges in practice. The Zeta potential of cationic Fe_3O_4 (m) and negatively charged GO nanosheets at pH 7.0 had $\approx+25$ and ≈-50 mV, respectively, **Figure 2a**. This large difference in charge ($\Delta\xi = 75$ mV) leads to strong electrostatic adsorption. The Zeta potential of $GO_{(m)}$ at pH 7.0 has been observed at ≈-60 mV, Figure 2a. After electrostatic adsorption, chemical reduction was conducted, leading to the generation of $rGO_{(m)}$, henceforth referred to as $rGO_{(m)}$. The successful attachment of Fe_3O_4 (m) nanoparticles on graphene sheets (electrostatic adsorption and short-range van der Waals attractions) was confirmed by transmission electron microscopy (TEM), Figure 1c. We briefly note that the concentration of Fe_3O_4 (m) nanoparticles was kept constant (0.003%) for all compositions.
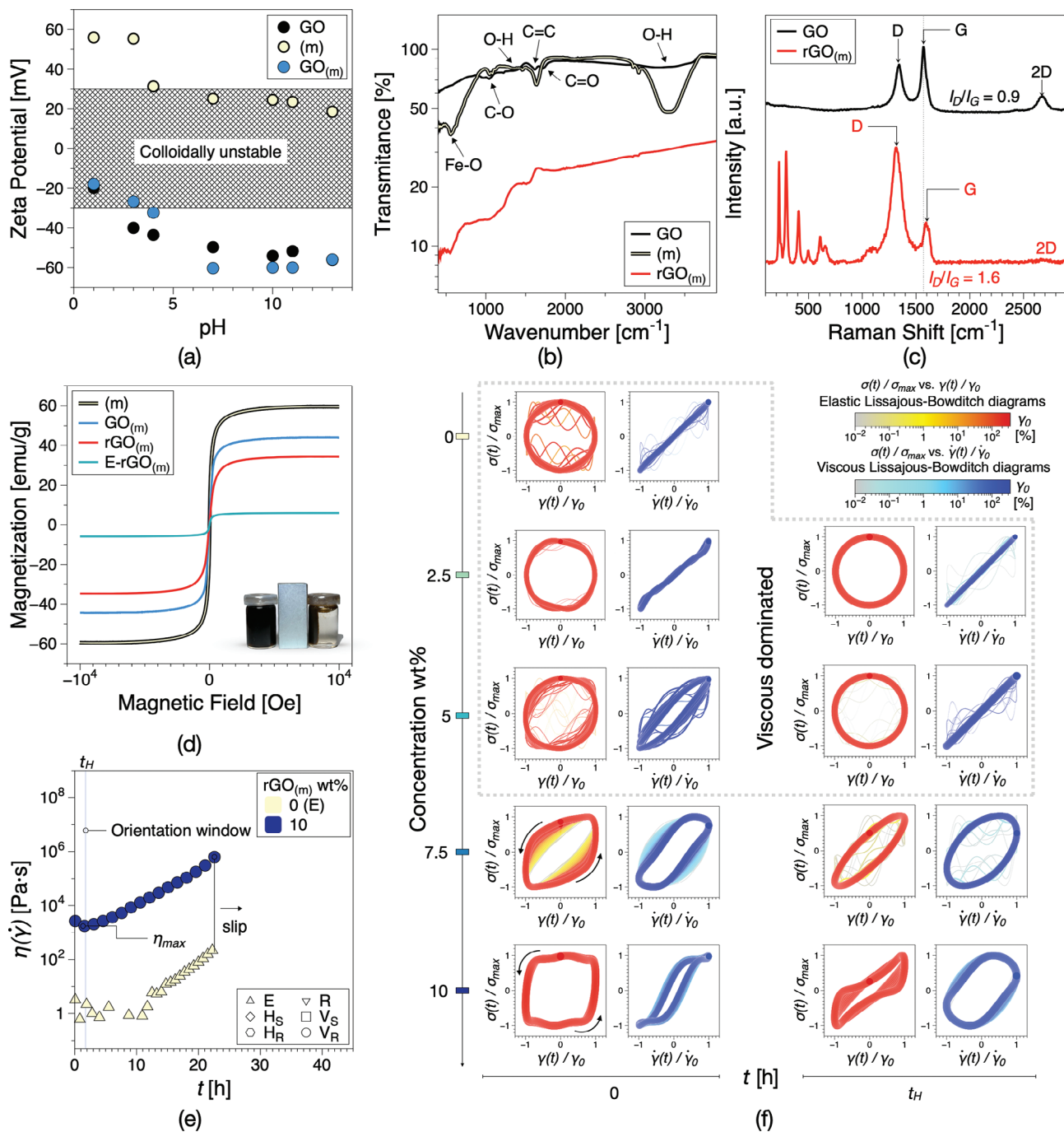
The reduction of GO to $rGO_{(m)}$ was confirmed by the reduction in oxygen-functional groups in $rGO_{(m)}$ in the Fourier transform infrared spectroscopy (FTIR) spectra, see Figure 2b. The skeletal vibration of aromatic (C = C), carboxyl (C = O) and hydroxyl (O–H) functional groups appears at 1620, 1718, and 3300 cm^{-1}, respectively in GO are significantly weakened or disappeared indicating that GO has been successfully reduced to $rGO_{(m)}$ chemically using the applied procedure, further appearing of a new peak (Fe–O) at 568 cm^{-1} shows the complete attachment of Fe_3O_4 (m) nanoparticles with rGO see Section S2 (Supporting Information) for further details. Subsequently, Raman spectroscopy and X-ray photoelectron microscopy (XPS) confirmed the structural transition from GO to $rGO_{(m)}$. In the Raman spectra, this was

2406875 (2 of 12)

**ADVANCED
SCIENCE NEWS**

www.advancedsciencenews.com

**ADVANCED
FUNCTIONAL
MATERIALS**

www.afm-journal.de

Figure 1. a) Composite image of the Halbach magnet array orientation cell and modeling of the magnetic scalar potential (contours) and normalized magnetic flux density (scalar plot). b) The various nanocomposite morphologies investigated in this study: (E) - epoxy (no fillers), (R) - random orientation (no magnetic field), (H) - 'horizontal' orientation configuration with the magnetic field lines oriented in-plane with the sample, (V) - 'vertical' orientation configuration with the orientation direction perpendicular with the sample plane. Indices $_S$ and $_R$ refer to static ($\Omega_m = 0$) and rotating magnetic fields ($\Omega_m > 600$ rpm; note: the sample is rotating while the magnet is stationary). c) TEM of reduced graphene oxide (rGO) before and after doping with Fe_3O_4 ($rGO_{(m)}$), and d) SEM of composite samples without fillers (E), with fillers without the application of a magnetic field (R), and oriented using Halbach array (H_S), (H_R), (V_S), and (V_R).

based on the increase in I_D/I_G ratio of $rGO_{(m)}$ to 1.6 compared to 0.9 for GO, see Figure 2c. This indicates the decrease in the average size of sp^2 carbon domains after the reduction; further, the presence of strong bonding of Fe_3O_4 in the magnetic graphene can be confirmed by the presence of signature peaks of Fe_3O_4 at 216, 277, and 667 cm^{-1}, see Section S3 (Supporting Information) for further details. Additionally, the transformation of GO to rGO is confirmed through XPS. The analysis revealed a notable increase in the atomic percentage of carbon from 78.4% to 91.3%, accompanied by a corresponding reduction in oxygen from 21.6% to 8.7%. Furthermore, the successful attachment of

Fe_3O_4 is confirmed through the detection of Fe2p at 711.0 eV. For more detailed information, please refer to Section S4 (Supporting Information). The magnetic hysteresis loop of all the characterized materials showed a sigmoid shape with a reversible behavior and no obvious coercivity, which is the typical superparamagnetic behavior, Figure 2d. Despite the comparatively lower saturation magnetizations of the fillers after their incorporation in the matrix, the inset image in the figure is a visual confirmation that an M_s of 34.2 emu g^{-1} was high enough to ensure the separation of $rGO_{(m)}$ in DI water under an external magnetic field compared to both Fe_3O_4 (m) (59.4 emu g^{-1}) and $GO_{(m)}$ (43.8 emu g^{-1}).

**ADVANCED
SCIENCE NEWS**

www.advancedsciencenews.com

**ADVANCED
FUNCTIONAL
MATERIALS**

www.afm-journal.de

Figure 2. Fundamental material characterization: a) Zeta potential of GO and Fe_3O_4 (m) as a function of pH. b) FTIR spectra of GO, Fe_3O_4 (m) and $rGO_{(m)}$. c) Raman spectra of GO and $rGO_{(m)}$ after reduction with hydrazine at 90 C. d) magnetization hysteresis loop at room temperature, illustrating the magnetic characteristics of the investigated materials. The inset of (d) highlights the separation behavior of $rGO_{(m)}$ in deionized (DI) water when exposed to an external magnetic field. e) curing kinetics from steady shear viscosity as a function of curing complementing the oscillatory shear time sweep in Figure S7a (Supporting Information) and f) Nonlinear material response analysis in the form of the beginning of the curing reaction and during orientation in the Halbach magnet array.

Rheological properties dictate the ability of the magnetic field to orient the nanofillers, how fast they orient and the timescale for de-orientation once samples are removed from the magnet, see Section S5 (Supporting Information) for further details. We estimate that shear viscosities of up to 10^3 Pa·s could be overcome within the 20 min orientation time to achieve highly oriented nanostructures, Figure 2e. Furthermore, the nonlinear material 'fingerprints' in the form of elastic, $\sigma(t)/\sigma_0$ versus $\gamma(t)/\gamma_0$ and viscous $\sigma(t)/\sigma_0$ versus $\dot{\gamma}(t)/\dot{\gamma}_0$ Lissajous–Bowditch (LB) diagrams, Figure 2f, show that
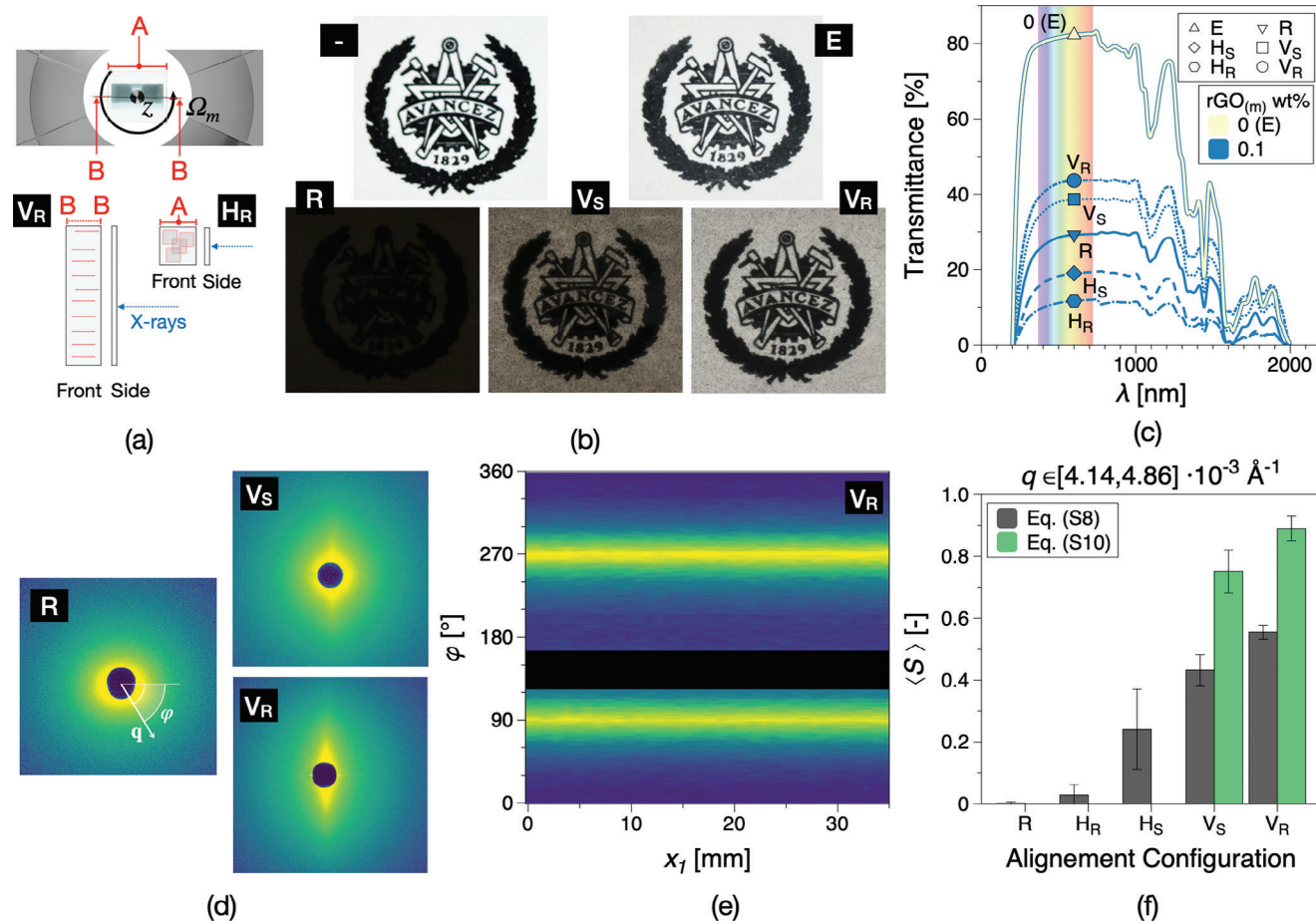
below 7.5 wt.% orientation is achieved in pure viscous systems (circular stress–strain in the elastic LB and linear stress–strain-rate response). In contrast, for concentrations over 7.5 wt.%, there is evidence that the orientation is achieved starting from the viscoelastic material response in percolated conditions (before orientation). This is substantiated by the similarity between the nonlinear 'fingerprints' at $t = 0$ to similar fingerprints identified at percolation in several previous studies on systems for which the matrix is Newtonian (pure viscous).[37,38] Whereas, for $t = t_H$ the nonlinear response is more similar to systems with viscoelastic matrices such as polymer melts.[39,40]

2.1. Anisotropy and Optical Properties

Several orientation configurations were considered in the study, as summarized in Figure 1b. We note that in magnetostatic conditions, the c-axis of the fillers is perpendicular to the magnetic field lines, leaving the angular positioning of their a-axis arbitrary within the graphene nanosheet's basal plane. Thus, given a static magnetic field of sufficient strength, graphene nanosheets will orient with the c-axis perpendicular to the magnetic field lines, Figure S4a (Supporting Information). Consequently, the a-axis can have any angular position with respect to the c-axis and graphene nanosheets and the basal plane can have any angular position around the a-axis. In contrast, in a rotating magnetic field of sufficient strength and angular frequency, $\Omega_m > 600$ rpm, the c-axis is perpendicular to the plane of rotation of the magnetic field and thus, the basal plane loses its degree of freedom around the a-axis, Figure S4b (Supporting Information). The latter case results in nanofillers parallel to the rotation planes formed by the magnetic field lines, also referred to as 'planar orientation'.[16] The morphological distinctions between horizontally (H_S) and vertically (V_S) aligned samples subjected to a static magnetic field are evident in the SEM micrographs in Figure 1d. Moreover, when the samples are subjected to a rotating magnetic field, the planar alignment of nanosheets in horizontal (H_R) and vertical (V_R) direction is clearly visible in Figure 1d and is further detailed in Section S6 (Supporting Information). We noted that there are multiple length scales present in the systems investigated: from filler agglomerates that are observable through optical microscopy, stacks of graphene basal planes due to incomplete exfoliation, and to local 'crumples' in the nanosheets, e.g., see the detail for (V_R) in Figure 1d, that can only be evidenced through probing nanoscale lengthscales. A first visual check of the high degree of orientation that includes contributions from all lengthscales smaller than the observation lengthscale (note the sample configuration in **Figure 3**a) can be performed using visible light, Figure 3b. It is readily observable that while the reference epoxy (E) being an amorphous polymer is highly translucent, 0.1 wt.% rGO$_{(m)}$ random orientation results in an opaque material. And in increasing order from (V_S) to (V_R) the test materials become increasingly translucent, for orientation perpendicular to the viewing direction. This is readily quantified via UV–vis–NIR spectroscopy, Figure 3c (0.1 wt.% rGO$_{(m)}$) and Section S7 (Supporting Information) for further details. Notably, the

samples aligned vertically in a rotating magnetic field (V_R) exhibited 60% and 16% higher light transmission compared to the randomly oriented (R) and statically oriented (V_S) counterparts. Conversely, when graphene nanosheets were aligned horizontally, a drastic reduction in light transmission was observed. Impressively, (H_R) demonstrated ≈42% higher light-blocking efficiency compared to (H_S), whereas the improvement in light transmission achieved through (V_R) was only ≈16% compared to (V_S). A noteworthy observation is the higher transmittance displayed by graphene sheets aligned vertically in comparison to their horizontally aligned counterparts (Figure 3b). For a description of anisotropy through further optical analysis, FTIR and Raman spectroscopy, refer to Sections S7, S2, and S3 (Supporting Information).

Representative scattering patterns from small-angle X-ray scattering (SAXS) readily show a isotropic pattern for (R) and an increased anisotropy from the magnetostatic to magnetodynamic induced orientations, Figure 3d. The long-range nanoscale structuring of the samples was tested by scanning along the vertical direction of the laboratory reference coordinate system, see Figure 3e. The data represented consists of an azimuthal integration of the scattering intensity, $I(\mathbf{q}, \varphi)$, (arbitrary units), where φ is the azimuthal angle within a given q-range. We note that in both representations the scattering data is presented in the reciprocal space and thus, the orientation peaks in e.g. Figure 3e correspond to orientation in the horizontal direction relative to the scattering patterns, however, their relative to the sample plane is vertical. Order parameters $<S>$, of up to 0.89 were obtained for the magnetodynamic orientation configuration, see Figure 3f. It is important to note that there are various frameworks for defining an order parameter, such as using via Lagrangian series fit[41,42] or via a Gaussian function fit, see Section S8 (Supporting Information). Depending on the choice and associated procedure, the order parameter can vary considerably, and in some cases, they are very difficult to obtain, see Figure 3f (note the absence of order parameter estimations from Gaussian fits for $H_{R, S}$). Furthermore, SAXS order parameters are characteristic of lengthscales that take into consideration local 'crumples' in the nanosheets, as opposed to microscopy-based order parameters.[26] With these considerations, regardless of the method, the highest degree of order at nanoscale is confirmed for $V_{R, S}$ highlighting their nanoscale planar orientation when compared to V_S. Horizontal samples in static conditions, H_S, being probed through incident X-rays perpendicular to their basal plane (refer to Figure 3a; Figure S4, Supporting Information) lacking planar orientation, show a distinguishable degree of order whereas V_R is indistinguishable from (R). The long-range nanoscale structuring of the samples was tested by scanning along the vertical direction of the laboratory reference coordinate system, see Figure 3e for V_R. The azimuthally-integrated scattering intensity remained unchanged throughout the distance interrogated, confirming the uniformity of the induced planar orientation in sample. Consequently, the findings presented collectively validate the multiscale and long-range consistent orientation of graphene within the Halbach array configuration when subjected to a magnetic field strength of 1 T and substantiate the expected morphological differences between the orientation configurations, Figure 1b.
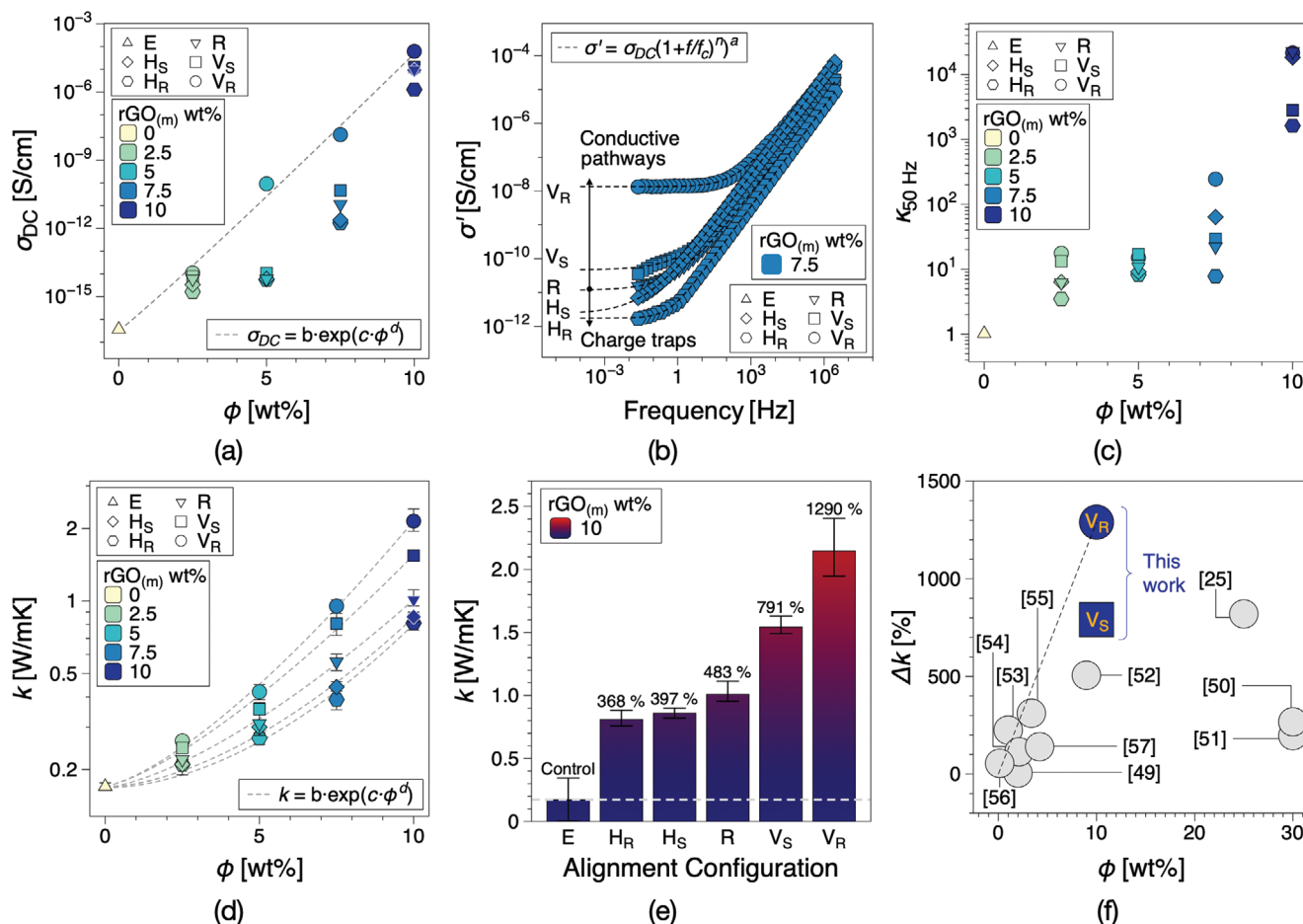
ADVANCED
SCIENCE NEWS

www.advancedsciencenews.com

ADVANCED
FUNCTIONAL
MATERIALS

www.afm-journal.de

Figure 3. a) Illustration of (V_R) and (H_R) orientation configurations prepared for anisotropy analysis. b) Optical images of samples illustrated in (a) showing a comparison between (R), (V_S) and (V_R) morphologies. c) Transmission spectra for epoxy (E) and graphene nanocomposite orientation morphologies with 0.1 wt.% $rGO_{(m)}$. d) Scattering patterns and azimuthal integration of the scattering intensity $I(\mathbf{q}, \varphi)$ (arbitrary units), as a function of scanning distance x_1, where q is the magnitude of the scattering vector, $|\mathbf{q}|$, and φ is the azimuthal angle. e) Example of long-range scan in the form of azimuthal integration for V_R, as function of the scanning direction, x_1. f) Nanoscale order parameter, $<S>$, comparing the alignment configurations studied using Hermans procedure and Gaussian fitting of the scattering intensity from azimuthal integration.

2.2. Electrical Properties

For most nanocomposite applications focused on electrical conductivity, the percolation threshold is a crucial parameter to assess the level of filler dispersion. In this context, nanocomposites capable of achieving percolation thresholds that approach theoretical levels are usually difficult to obtain and/or require substantial nanofiller surface modifications.[43] Referring to percolation thresholds, this usually presumes a random filler nanocomoposite morphology. However, for the vast majority of applications, a certain level of orientation is unavoidable during manufacturing, which can disrupt percolated networks.[44] Furthermore, in some cases, the orientation direction induced during manufacturing will not be favorable to create desirable effects, such as e.g., conductive pathways or nonlinear field-dependent behavior.[45,46] Therefore, the ability to induce a high level of long-range nanofiller orientation in an arbitrary direction is of paramount importance for most applications. **Figure 4**a illustrates the electrical conductivity as extrapolated from the dielectric spectra in the limit of low AC frequencies, see also Section S9 (Supporting Information). Based on (R), a notable surge in DC conductivity exceeding three orders of magnitude is observed starting with 7.5 wt.%, potentially suggesting the onset of a percolation behavior.[46] This is in the range of percolation thresholds reported for various nanocomposites (5–12%) even in the absence of network disruptions due to orientation and for systems with relatively low dispersion levels.[43] Below 7.5 wt.%, $(H_{S, R})$, and (V_S), have an indistinguishable effect on the electrical conductivity compared to (R). However, starting with 7.5 wt.% a clear distinction between the orientation configuration clearly emerges, see Figure 4b. For systems with horizontal orientation, the presence of graphene perpendicular to the direction of an applied electric field is expected to lead to charge traps at low electric fields, thus reducing the transport of electric charges, effect that should be more significant for higher applied electric fields.[45] Significantly, all (V_R) samples, regardless of $rGO_{(m)}$ concentration, exhibited a quasi-'linear' functional dependence (note the log-lin dependence, see also Equation (S5), Supporting Information for $d = 1$). This leads to a remarkable relative increase in electrical conductivity, reaching up to four decades when compared to

**ADVANCED
SCIENCE NEWS**

www.advancedsciencenews.com

**ADVANCED
FUNCTIONAL
MATERIALS**

www.afm-journal.de

Figure 4. a) DC conductivity, σ_{DC}, variation with filler content as determined from the dielectric spectra in Figure S10 and Equation (S5) (Supporting Information). b) Dielectric spectra for 7.5 wt.% in the form of the real part of the electrical conductivity, σ', highlighting the formation of conductive pathways and charge traps depending on the orientation configuration. c) Dielectric constant (at ≈ 50 Hz) as a function of filler content. d) Thermal conductivity, k, as a function of filler content. e) Increase in thermal conductivity (and percentage improvement) for 10 wt.% compared to (E). f) Percentage improvement in thermal conductivity compared to similar studies.

(R). Notably, no discernible typical percolation threshold was observed in the (V$_R$) samples. These findings surpass those reported in the literature, where the maximum increase in alignment is documented to be up to three decades compared to (R), again with no discernible percolation threshold.[47] To validate this phenomenon, the results were replicated three times. This could imply the formation of a conductive rGO$_{(m)}$ network at concentrations as low as 2.5 wt.% in a rotating magnetic field. It could be that the magnetic force exerted on the fillers could cause displacement of the fillers in the direction of the magnetic field resulting in long string-like formations to reduce hydrodynamic drag, compensating for the loss of connectivity due to orientation.[47] A consequence could be the possibility of line or partial overlap 'contact' between graphene nanosheets for planar orientation whereas in static conditions point contacts would be prevalent. The (V$_R$) 10 wt.% sample showed the highest electrical conductivity, reaching the significant value of 6.2×10^{-5} S cm^{-1}. Moreover, the (V$_R$) 10 wt.% samples demonstrated the highest dielectric constant among all 10 wt.% samples, indicating promising applications in high-energy-density capacitors where a high relative dielectric constant is imperative, see Figure 4c. This outcome

is attributed to improved interfacial interaction between rGO$_{(m)}$ and epoxy, along with enhanced rGO$_{(m)}$ distribution, resulting in reduced polarization relaxation and consequently a high dielectric constant compared to the other orientation configurations. It's noteworthy that the dielectric loss of the 10 wt.% sample, as illustrated in Figure S10f (Supporting Information), is maximized due to its higher electrical conductivity relative to other samples, see also Equation (S6) (Supporting Information). Finally, it is worth mentioning that although the focus of the discussion has been on maximizing the electrical conductivity, horizontally oriented samples could also lead to more pronounced nonlinear field grading behavior due to the high level of orientation perpendicular to an applied electric field.

2.3. Thermal Properties

Similarly to electrical conductivity, thermal conductivity is also significantly influenced by the orientation configurations studied, Figure 4d. As phonon scattering is the mechanism for the transfer of thermal energy, interfaces in a composite play a

**ADVANCED
SCIENCE NEWS**

www.advancedsciencenews.com

**ADVANCED
FUNCTIONAL
MATERIALS**

www.afm-journal.de

significant role in their thermal conductivity.[48] Therefore, thermal conductivity is less susceptible to electrical percolation and the existence of a thermal percolation remains controversial.[49] This appears to be the case in the present study as well as evidenced by their monotonic functional dependence on the filler concentration independently of the orientation configuration. Upon subjecting the rGO$_{(m)}$ composites to the Halbach array, an anisotropic thermal conductivity was observed, with a clear trend $V_R > V_S > R > H_S > H_R$. The maximum thermal conductivity was attained as expected for (V_R) at 10 wt.%, reaching 2.41 W mK^{-1}. This is a 1290% improvement over the epoxy reference (E) and ca. 200% compared to (H_R) at the same concentration, Figure 4e. The preparation of a vertically oriented sample under a uniform rotating magnetic field generated by a Halbach array clearly stands out among similar studies as the highest attained improvement in thermal conductivity, Figure 4f.[50–58] Furthermore, it is worth highlighting that even in magnetostatic conditions, V_S reaches thermal conductivity enhancements comparable to some systems containing over twice as much nanofiller. While we emphasized the relevance of rotating magnetic fields in terms of alignment and subsequent performance, it is worth noting that the importance of the static versus dynamic alignment of the nanofillers is relative to the application targeted and therefore contributes to the versatility of the method.

2.4. Antibacterial Properties

To strengthen the new possibilities offered by the Halbach array orientation method we refer to one of the challenges humanity is likely to face, according to the United Nations: antimicrobial resistance.[59] A critical aspect related to this challenge is to limit Healthcare-related infections (HAI) by designing highly efficient antibacterial surfaces that could be incorporated in various medical devices. Previously, we had developed polymer nanocomposite surfaces based on graphite nanoplatelets capable of reducing antibacterial viability by a factor of 99%, which remains the benchmark in the field.[19,60] The critical enabler of such high performance are the high level of orientation and density of distribution of exfoliated graphite nanoplatelets within the polymer nanocomposite.[61] This was achieved by tailoring the extrusion processing window of the nanocomposites, followed by slicing and etching of the sample to expose the edges of the fillers. Crucially, human cells due to their larger size, remain unharmed by the surfaces.[9] The major challenge for actually developing medical devices using the technology is related to the crux of the present study: flow-induced orientation leads to in-plane orientation of the fillers (horizontal) while most applications would require an orientation of the nanofillers perpendicular to the flow direction. Thus, aligned graphene nanosheets (10 wt.%) samples were subjected to 30-min etching in H$_2$SO$_4$ to remove epoxy and expose sharp graphene edges. Indeed, the vertically rotating (V_R) configuration displays exceptional antibacterial efficacy at 99% against both strains, **Figure 5a–c**, see also Section S10 (Supporting Information). Thus, the Halbach array-oriented samples are capable of reaching similar levels of antibacterial efficacy as in our previous study, while reducing the filler content by up to 50%. In addition to the orientation and density, the doped nanoparticles on the surface of graphene can further contribute to antibac-

terial efficacy by oxidizing the cell membrane through the generation of reactive oxygen species (ROS) or direct electron transfer, particularly in the case of (V_R). Additionally, preventing bacterial attachment to the surface is crucial for overall effectiveness. A hydrophobic surface with a contact angle of 143° and 121° is observed in the prepared (V_R) and (V_S) samples, Figure 5d, while horizontally aligned (H_R) and (H_S) samples exhibit a hydrophilic surface with a contact angle of 27° and 34°. This distinction in surface properties influences the initial interaction of bacteria with the surface, impacting both bacterial attachment and subsequent killing efficiency. A hydrophobic surface not only deters bacterial attachment but also aids in the removal of any attached bacteria by 'nano-knives', preventing the deposition of dead bacteria and maintaining surface efficiency. And finally, taking into consideration the electro-thermal properties outlined in the previous sections, synergetic effects could be envisioned to further enhance antibacterial effects through sensorics and using temperature as a potential additional factor toward antibacterial effects. We therefore conclude that the synergistic action of these phenomena could result in an antibacterial technology of unparalleled potential.

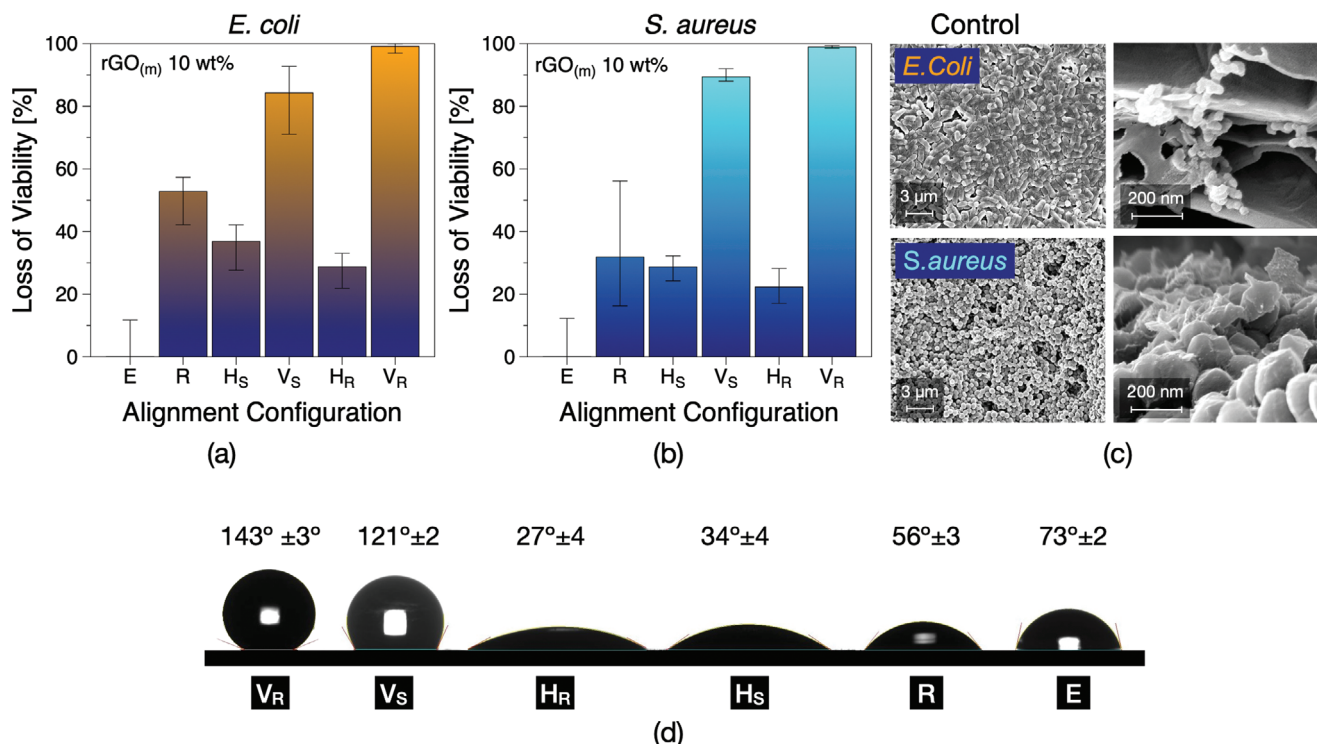### 2.5. Halbach Array: Orientation Powerhouse

As illustrated in the current study, the Halbach array demonstrates a remarkable capacity for achieving ultra-high orientation of 2D nanosheets, specifically graphene. We wish to briefly mention that while the present study being focused on graphene, the method developed has far-reaching implications for any anisotropic nanofillers and even macro-fillers. We exemplify this briefly on 1D cellulose nanocrystals (chiral nematic phase), carbon nanotubes (CNT) and wood fibers, **Figure 6**, using, the same filler doping and optimization procedures. Furthermore, even spherical nanoparticles (0D, SN), such as Fe$_2$O$_3$, exhibit a fascinating behavior–arranging themselves in elongated agglomerate strands under the influence of the magnetic field produced by the Halbach array.

3. Conclusion

In light of these discoveries, the tailored implementation of the Halbach array emerges as a powerful tool for fabricating complex hierarchical structures. The ability to precisely control the orientation of nano- and micro-sized particles across different dimensions open the door to innovative possibilities in materials science and engineering. This study not only contributes to understanding the Halbach array's capabilities but also lays the foundation for designing and fabricating intricate structures for diverse applications.

4. Experimental Section

Synthesis of Magnetic Graphene:: To initiate the synthesis of magnetically responsive graphene nanosheets, Graphene Oxide P935, procured from LayerOne in Norway, was chosen as the primary material. The graphene oxide was first dispersed in deionized water at a concentration of 10 mg mL^{-1}. Subsequently, the dispersion underwent functionalization

ADVANCED
SCIENCE NEWS

www.advancedsciencenews.com

ADVANCED
FUNCTIONAL
MATERIALS

www.afm-journal.de

Figure 5. Loss of antibacterial viability on 10 wt.% rGO$_{(m)}$ etched nanocomposite surfaces against a) Gram-negative and b) Gram-positive bacteria. c) SEM showing the tested bacteria growing on the Control (E) surface compared to the absence of bacteria and the presence of significant amounts of dead bacteria on the V$_R$ surface. d) Water contact angle measurements on prepared the antibacterial surfaces e) Structuring of 1D cellulose nanocrystals (CNC) chiral nematic phase, 1D carbon nanotubes (CNT) nanofillers, micro-fillers / 3D nanofillers (wood fibers, WF) and 0D spherical nanoparticles (SN; Fe$_2$O$_3$) using the Halbach array setup.

with a cationic-type ferrofluid (EMG 605, Ferrotech, USA) at a neutral pH of 7 through electrostatic adsorption. Maintaining a constant ferrofluid concentration of 0.003% throughout the process, the prepared mixture was vigorously stirred at 400 rpm for 10 min. This was followed by a meticulous 15-min sonication process to ensure the complete adsorption of the ferrofluid onto the graphene oxide sheets. To achieve a reduction of GO, hydrazine (2mg mL^{-1}) was introduced into the solution, which was then sonicated for an additional 30 min. The resultant mixture was subjected to controlled heating at 90°C for a duration of 2 h, which lead to the formation of magnetically responsive reduced graphene oxide (rGO$_{(m)}$). The visually distinctive black powder (rGO$_{(m)}$) sediments were then subjected to washing in deionized (DI) water using a centrifugation technique. Subsequently, the washed material underwent a freeze-drying process to yield the final magnetic-responsive rGO$_{(m)}$ powder.

Composite Fabrication: For detailed optical studies, the magnetically responsive reduced graphene oxide (rGO$_{(m)}$) prepared at a concentration of 0.1 wt.% was introduced into a meticulously blended 74% epoxy (cast epoxy, Carbix, Sweden) and 26% hardener resin composition. The amalgamation underwent a thorough 5-min mixing process, followed by 15-min sonication to achieve a uniformly dispersed rGO$_{(m)}$ within the epoxy matrix. The resulting solution was carefully poured into a silicon mold and, if necessary, subjected to alignment within a Halbach array under either a static or rotating magnetic field for 20 min. Then, the composite was left to cure at room temperature for 24 h, after which it was removed and cured at 100°C for an additional 24 h to ensure the complete curing of the fabricated composite. For investigations into thermal and electrical conductivity, a similar procedure was followed, with the rGO$_{(m)}$ concentrations between 2.5 and 10 wt.%. For antibacterial studies, 10 wt.%
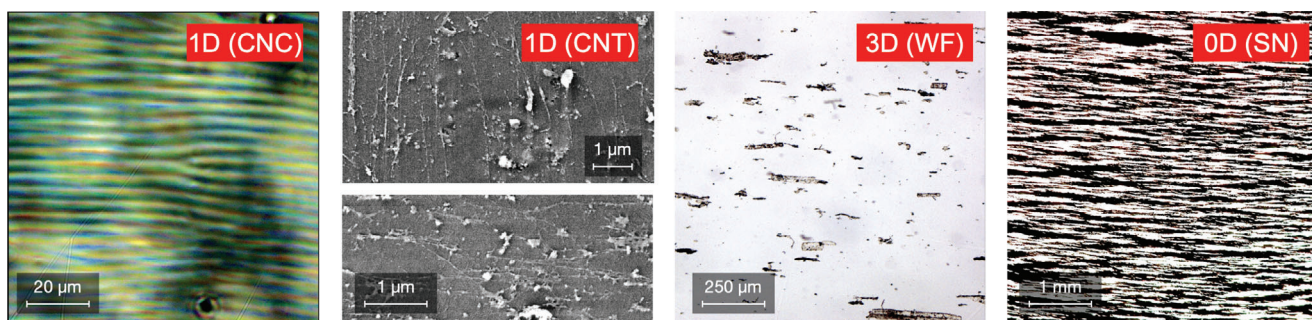
Figure 6. Structuring of 1D cellulose nanocrystals (CNC) chiral nematic phase, 1D carbon nanotubes (CNT) nanofillers, micro-fillers / 3D nanofillers (wood fibers, WF) and 0D spherical nanoparticles (SN; Fe$_2$O$_3$) using the Halbach array setup.

samples were prepared using the aforementioned procedure to generate sharp nano-knives of graphene within the composite. The resultant composite was subsequently etched for 30 min in H_2SO_4 under a constant rotation speed of 600 rpm. Following the etching process, the composite underwent a thorough washing at least five times in deionized (DI) water to ensure the complete removal of residual acid.

Zeta potential: Zeta potential measurements of graphene and Fe_3O_4 (m) suspensions were performed using a Zetasizer Nano ZS (Malvern Instruments, UK) with DTS1070 folded capillary cells. Both the suspensions were diluted to 0.01 wt.%, and all the measurements were conducted at 23°C, with a stabilization time of 120 s, repeated three times, and the average value was reported.

TEM and SEM: Bright-field TEM (BF-TEM) images were collected on an FEI Tecnai T20 microscope, equipped with a LaB6 filament and operating at 200 keV acceleration voltage. Both GO and rGO$_{(m)}$ samples were deposited on commercial electron-transparent substrates consisting of a holey-carbon film on a copper grid (Ted Pella, Inc). The surface morphology of prepared composites after etching and the size of graphene nanosheets and Fe_3O_4 nanoparticles were analyzed in a secondary electron (SE) mode using LEO 1550 Gemini field emission gun SEM (FEG-SEM).

Raman spectroscopy: Raman spectra were recorded on a WITec alpha300 R Raman spectrometer with a 532 nm laser line. For Raman analysis, powder samples were placed on the surface of the glass slide and firmly pressed for a homogeneous consistency.

FTIR and XPS: Fourier-transform infrared spectroscopy (FTIR) was performed using a PerkinElmer Spectrum One instrument equipped with an attenuated total reflectance (ATR). A background of air was collected prior to the measurements, and the samples were placed on top of the ATR crystal and secured using a metal clamp to ensure consistent pressure. The device was set to collect the spectra in a transmittance mode between 4000 and 400 cm^{-1}, with 32 scans being collected with a resolution of 2 cm^{-1}. XPS analysis was performed using a PHI 5000 VersaProbe III Scanning XPS Microprobe (Physical Electronics, Feldkirchen, Germany) at an angle of 45°. The graphene oxide and reduced graphene powders with and without Fe_3O_4 nanoparticles were drop casted on the silicon wafers and subjected to the XPS analysis.

Magnetization Hysteresis Loops: A MicroMag 2900 alternating gradient magnetometer (AGM) was used to characterize the magnetic properties of the samples. Samples were prepared on the silicon (Si) substrate. The substrates were weighed both before and after the deposition of samples to determine the exact weight of the samples with a precision of up to four decimal places. Further, the samples prepared on the Si substrates were attached to the probe using vacuum grease. Magnetization curves were obtained in in-plane field sweep mode from 10^4 to 10^{-4} Oe at room temperature. The built-in linear slope correction was performed after the measurement.

Rheological Characterization: An Anton Paar MCR702e Space and MCR702 TwinDrive (Graz, Austria) rotational rheometers were used. Steady shear (shear rate: $\dot{\gamma} = 10^{-3}$ s^{-1}) and linear viscoelastic oscillatory shear tests (strain amplitude and angular frequency: $\gamma_0 = 10^{-1}$%, $\omega = 6.28$ rad s^{-1}) were performed in single motor-transducer configuration while the nonlinear analysis was performed in separate motor-transducer configuration using strain amplitude sweep tests ($\omega = 1$ rad s^{-1}). Parallel-plate measuring geometries were used of 25 and 50 mm in diameter depending on the torque output. For the strain sweep tests, the time-dependent shear stress response, $\sigma(t)$ was recorded as a simple insight into the nonlinear material behavior of the test materials at the beginning of the curing reaction, $t = 0$, and the time corresponding to their insertion in the Halbach array for orientation, $t = t_H$, see Figure S7f (Supporting Information). Further details can be found in Section S5 (Supporting Information).

UV–vis–NIR: UV–vis–NIR spectroscopy of prepared composites was performed on a PerkinElmer Lambda 1050 UV–vis–NIR spectrophotometer, using air as a background from 300 to 2100 nm wavelength.

Small-Angle X-Ray Scattering (SAXS): SAXS experiments were performed at the CoSAXS beamline,[62] MAX IV Laboratory, Lund University, Sweden. Linear scans were performed with the incident beam perpendicular to the sample plane (see Figure 3e) over a maximum total length of ca. 35 mm with a distance increment of ≈0.71 mm and an exposure time of 0.1 s. Order parameters, $<S>$, were determined from azimuthally integrated SAXS data using the Hermans procedure, see Equation (S1) (Supporting Information) and via Gaussian function fitting, see Equation (S3) (Supporting Information). The azimuthal data was binned in several q-range increments and the orientation parameters were averaged over $q \in$ [4.14, 4.86] · 10^{-3} Å^{-1} for several samples.

Dielectric Spectroscopy: A Novocontrol Alpha spectrometer was used to determine the dielectric spectra and subsequently the DC conductivity in the limit of low frequencies, $\sigma_{DC} = \lim_{f \to 0} \sigma' f$, where σ' is the real part of the electrical conductivity, as determined from the imaginary part of the dielectric permittivity.

Thermal Conductivity: Thermal conductivity was measured using Hot Disk TPS 2500S thermal analyzer (Hot Disk AB, Göteborg, Sweden). The measurement proceeds by selecting the appropriate heating power, measurement time and sensor type. For the current work, a Hot disk sensor with radii of 0.526 was used for all the measurements. All the measurements were carried out at room temperature.[46]

Antibacterial Testing: The bacterial strains *Escherichia coli* (UTI89) and *Syaphylococcus aureus* (CCUG10778) were obtained from Gothenburg University Culture Collection (CCUG) and used to evaluate the antimicrobial potential of epoxy (control) and rGO incorporated epoxy samples. The culture medium Luria-Bertani (LB) broth and tryptic soy broth (TSB) were used to culture *E. coli* and *S. aureus*, respectively. Single colonies of each bacterial strain were grown in a liquid medium at 37°C overnight. Then, an inoculum containing $2 - 5 \times 10^6$ CFU mL^{-1} bacteria was prepared by diluting the overnight bacterial culture in fresh medium. A fraction of the inoculum was placed on the surface of control and rGO$_{(m)}$ incorporated epoxy samples. The inoculum loaded samples were incubated for 24 h at 37 °C. After 24 h bacterial growth samples were collected in 5 mL of 0.89% of NaCl and attached bacterial cells were detached from surfaces by means of sonication (10% amplitude, 30 sec). The homogenized bacterial cells in 0.89% of NaCl were further diluted serially and plated in agar plates to count the colony forming unites (CFUs). For SEM, attached bacterial cells on surfaces were fixed by 3% glutaraldehyde at room temperature for 2 h, and dehydrated by graded series of ethanol (40%, 50%, 60%, 70%, 80%, and 90%) for 10 min each and by absolute ethanol for 15 min. The dehydrated samples were dried overnight at room temperature and sputter coated with 5 nm of gold layer before acquiring images.

Contact Angle Measurements: The surface wettability of epoxy (control) and rGO$_{(m)}$ incorporated epoxy samples were evaluated by measuring the water contact angle in air using an optical goniometer (OneAttension, Biolin Scientific). The needle diameter was 0.718 mm and images were taken within 1–2 s of the droplet (≈ 5 µL in size) being dispensed on the sample.

Supporting Information

Supporting Information is available from the Wiley Online Library or from the author.

Acknowledgements

**ADVANCED
SCIENCE NEWS**

www.advancedsciencenews.com

**ADVANCED
FUNCTIONAL
MATERIALS**

www.afm-journal.de

Conflict of Interest

The authors declare no conflict of interest.

Data Availability Statement

The data that support the findings of this study are available from the corresponding author upon reasonable request.

Keywords

[1] S. Sasidharan, A. Anand, *Ind. Eng. Chem. Res.* **2020**, *59*, 12617.

[2] A. C. Ferrari, F. Bonaccorso, V. Fal'Ko, K. S. Novoselov, S. Roche, P. Bøggild, S. Borini, F. H. Koppens, V. Palermo, N. Pugno, J. A. Garrido, R. Sordan, A. Bianco, L. Ballerini, M. Prato, E. Lidorikis, J. Kivioja, C. Marinelli, T. Ryhänen, A. Morpurgo, J. N. Coleman, V. Nicolosi, L. Colombo, A. Fert, M. G. Hernandez, A. Bachtold, G. F. Schneider, F. Guinea, C. Dekker, M. Barbone, et al., *Nanoscale* **2015**, *7*, 4598.

[3] K. Gong, K. Zhou, X. Qian, C. Shi, B. Yu, *Composites Part B* **2021**, *217*, 108867.

[4] S. Zheng, Y. Wang, Y. Zhu, C. Zheng, *Mater. Today Commun.* **2023**, *36*, 106773.

[5] Y. Gogotsi, B. Anasori, *ACS Nano* **2019**, *13*, 8491.

[6] Z. Wu, E. Wang, G. Zhang, Y. Shen, G. Shao, *Small* **2023**, *20*, 2307923.

[7] V. Ghai, K. Chatterjee, P. K. Agnihotri, *Carbon Lett.* **2021**, *31*, 473.

[8] P. Zhang, J. Li, L. Lv, Y. Zhao, L. Qu, *ACS Nano* **2017**, *11*, 5087.

[9] S. Pandit, Z. Cao, V. R. S. S. Mokkapati, E. Celauro, A. Yurgens, M. Lovmar, F. Westerlund, J. Sun, I. Mijakovic, *Adv. Mater. Interfaces* **2018**, *5*, 1701331.

[10] V. Ghai, H. Singh, P. K. Agnihotri, *ACS Appl. Opt. Mater.* **2022**, *1*, 252.

[11] V. Ghai, H. Singh, P. K. Agnihotri, *J. Appl. Polym. Sci.* **2020**, *137*, 48855.

[12] C. Deng, P. Gao, L. Lan, P. He, X. Zhao, W. Zheng, W. Chen, X. Zhong, Y. Wu, L. Liu, J. Peng, Y. Cao, *Adv. Funct. Mater.* **2019**, *29*, 1907151.

[13] S. Xu, J. Zhang, *Small Struct.* **2020**, *1*, 2000034.

[14] B. Su, Y. Wu, L. Jiang, *Chem. Soc. Rev.* **2012**, *41*, 7832.

[15] H. He, L. Guan, H. Le Ferrand, *J. Mater. Chem. A* **2022**, *10*, 19129.

[16] V. Ghai, S. Pashazadeh, H. Ruan, R. Kádár, *Prog. Mater Sci.* **2024**, *143*, 101251.

[17] V. Calabrese, S. J. Haward, A. Q. Shen, *Macromolecules* **2021**, *54*, 4176.

[18] C. Zhao, P. Zhang, J. Zhou, S. Qi, Y. Yamauchi, R. Shi, R. Fang, Y. Ishida, S. Wang, A. P. Tomsia, *Nature* **2020**, *580*, 210.

[19] S. Pandit, K. Gaska, V. R. Mokkapati, E. Celauro, A. Derouiche, S. Forsberg, M. Svensson, R. Kádár, I. Mijakovic, *Small* **2020**, *16*, 1904756.

[20] S. Wu, R. B. Ladani, J. Zhang, E. Bafekrpour, K. Ghorbani, A. P. Mouritz, A. J. Kinloch, C. H. Wang, *Carbon* **2015**, *94*, 607.

[21] H. Le Ferrand, S. Bolisetty, A. F. Demirörs, R. Libanori, A. R. Studart, R. Mezzenga, *Nat. Commun.* **2016**, *7*, 12078.

[22] B. Zhou, J. Zou, Z. Lin, Z. Yuan, X. Qin, P. Chen, D. Ye, *Chem. Eng. J.* **2023**, *457*, 141167.

[23] B. Yang, N. Jia, X. Wang, Y. Pan, M. Luo, X. Chen, R. Xia, Z. Zheng, J. Qian, Y. Ke, L. Su, Y. Fang, *Macromol. Mater. Eng.* **2022**, *307*, 2200144.

[24] F. Lin, Z. Zhu, X. Zhou, W. Qiu, C. Niu, J. Hu, K. Dahal, Y. Wang, Z. Zhao, Z. Ren, D. Litvinov, Z. Liu, Z. M. Wang, J. Bao, *Adv. Mater.* **2017**, *29*, 1604453.

[25] J. H. Ryu, S. M. Yang, J. U. Lee, J. H. Kim, S. J. Yang, *Carbon Lett.* **2022**, *32*, 1433.

[26] F. Lin, G. Yang, C. Niu, Y. Wang, Z. Zhu, H. Luo, C. Dai, D. Mayerich, Y. Hu, J. Hu, X. Zhou, Z. Liu, Z. M. Wang, J. Baoet, *Adv. Funct. Mater.* **2018**, *28*, 1805255.

[27] M. Dai, Y. Zhai, L. Wu, Y. Zhang, *Carbon* **2019**, *152*, 661.

[28] K. S. Novoselov, A. K. Geim, S. V. Morozov, D. Jiang, M. I. Katsnelson, I. V. Grigorieva, S. Dubonos, AA. Firsov, *Nature* **2005**, *438*, 197.

[29] K. S. Novoselov, A. K. Geim, S. V. Morozov, D. Jiang, Y. Zhang, S. V. Dubonos, I. V. Grigorieva, A. A. Firsov, *Science* **2004**, *306*, 666.

[30] S. K. Tiwari, S. Sahoo, N. Wang, A. Huczko, *J. Sci. Adv. Mater. Devices* **2020**, *5*, 10.

[31] J. Wu, H. Lin, D. J. Moss, K. P. Loh, B. Jia, *Nat. Rev. Chem.* **2023**, *7*, 162.

[32] S. S. Zalesskiy, E. Danieli, B. Blümich, V. P. Ananiko, *Chem. Rev.* **2014**, *114*, 5641.

[33] K.-F. Ratzsch, R. Kádár, I. Naue, M. Wilhelm, *Macromol. Mater. Eng.* **2013**, *298*, 1124.

[34] K.-F. Ratzsch, C. Friedrich, M. Wilhelm, *J. Rheol.* **2017**, *61*, 905.

[35] S. Tewari, T. O'Reilly, A. Webb, *J. Magn. Reson.* **2021**, *324*, 106923.

[36] A. Telfah, A. Bahti, K. Kaufmann, E. Ebel, R. Hergenröder, D. Suter, *Sci. Rep.* **2023**, *13*, 21092.

[37] S. Wojno, M. Fazilati, T. Nypelö, G. Westmand, R. Kádár, *Cellulose* **2023**, *29*, 3655.

[38] S. Wojno, A. Ahlinder, A. Altskär, M. Stading, T. Abitbol, R. Kádár, *Carbohydr. Polym.* **2023**, *308*, 120622.

[39] R. Kádár, K. Gaska, T. Gkourmpis, *Rheol. Acta* **2020**, *59*, 333.

[40] K. Gaska, R. Kádár, *AIP Conf. Proc.* **2019**, *2107*, 050003.

[41] P. Hermans, P. Platzek, *Kolloid-Z.* **1939**, *1*, 68.

[42] A. Rodriguez-Palomo, V. Lutz-Bueno, X. Cao, R. Kádár, M. Andersson, M. Liebe, *Small* **2021**, *17*, 2006229.

[43] T. Gkourmpis, K. Gaska, D. Tranchida, A. Gitsas, C. Müller, A. Matic, R. Kádár, *Nanomaterials* **2019**, *9*, 1766.

[44] R. Kádár, M. Abbasi, R. Figuli, M. Rigdahl, M. Wilhelm, *Nanomaterials* **2017**, *7*, 23.

[45] K. Gaska, X. Xu, S. Gubanski, R. Kádár, *Polymers* **2017**, *9*, 1.

[46] K. Gaska, R. Kádár, A. Rybak, A. Siwek, S. Gubanski, *Polymers* **2017**, *9*, 294.

[47] S. Wu, R. B. Ladani, J. Zhang, E. Bafekrpour, K. Ghorbani, A. P. Mouritz, A. J. Kinloch, C. H. Wang, *Carbon* **2015**, *94*, 607.

[48] K. M. Shahil, A. A. Balandin, *Solid State Commun.* **2012**, *152*, 1331.

[49] X. Huang, C. Zhi, Y. Lin, H. Bao, G. Wu, P. Jiang, Y.-W. Mai, *Mater. Sci. Eng., R* **2020**, *142*, 100577.

[50] D. Yao, N. Peng, Y. Zheng, *Compos. Sci. Technol.* **2018**, *167*, 234.

[51] C. Hu, H. Zhang, N. Neate, M. Fay, X. Hou, D. Grant, F. Xu, *Polymers* **2022**, *14*, 2583.

[52] J. Geng, Y. Men, C. Liu, X. Ge, C. Yuan, *RSC Adv.* **2021**, *11*, 16592.

[53] Y. Liu, M. Lu, M. Wu, S. Yao, X. Du, G. Chen, Q. Zhang, L. Liang, M. Lu, *Compos. Sci. Technol.* **2019**, *174*, 1.

[54] J. Renteria, S. Legedza, R. Salgado, M. Balandin, S. Ramirez, M. Saadah, F. Kargar, A. Balandin, *Mater. Des.* **2015**, *88*, 214.

[55] H. Yan, R. Wang, Y. Li, W. Long, *J. Electron. Mater.* **2015**, *44*, 658.

**ADVANCED
SCIENCE NEWS**

www.advancedsciencenews.com

**ADVANCED
FUNCTIONAL
MATERIALS**

www.afm-journal.de

[56] J. He, H. Wang, Q. Qu, Z. Su, T. Qin, X. Tian, *Compos. Manuf.* **2020**, *139*, 106062.

[57] Z. Wu, J. Chen, Q. Li, D.-H. Xia, Y. Deng, Y. Zhang, Z. Qin, *Materials* **2021**, *14*, 2013.

[58] H. Yan, Y. Tang, W. Long, Y. Li, *J. Mater. Sci.* **2014**, *49*, 5256.

[59] Bracing for superbugs: Strengthening environmental action in the one health response to antimicrobial resistance, Technical report, United Nations Environment Programme, Geneva **2023**.

[60] S. Pandit, K. Gaska, R. Kádár, I. Mijakovic, *Chem. Phys. Chem* **2021**, *22*, 250.

[61] S. Rahimi, T. Lovmar, A. Aulova, S. Pandit, M. Lovmar, S. Forsberg, M. Svensson, R. Kádár, I. Mijakovic, *Nanomaterials* **2023**, *13*, 10.

[62] M. Kahnt, K. Klementiev, V. Haghighat, C. Weninger, T. S. Plivelic, A. E. Terry, A. Björling, *J. Synchrotron Radiat.* **2021**, *28*, 1948.